

The effect of non-Gaussianity on error predictions for the Epoch of Reionization (EoR) 21-cm power spectrum

Rajesh Mondal^{1,2*}, Somnath Bharadwaj^{1,2†}, Suman Majumdar³,
Apurba Bera¹ and Ayan Acharyya¹

¹*Department of Physics, Indian Institute of Technology, Kharagpur - 721302, India*

²*Centre for Theoretical Studies, Indian Institute of Technology, Kharagpur - 721302, India*

³*Department of Astronomy & Oskar Klein Centre, AlbaNova, Stockholm University, SE-106 91 Stockholm, Sweden*

Accepted 2015 January 20. Received 2014 December 14; in original form 2014 September 15

ABSTRACT

The Epoch of Reionization (EoR) 21-cm signal is expected to become increasingly non-Gaussian as reionization proceeds. We have used semi-numerical simulations to study how this affects the error predictions for the EoR 21-cm power spectrum. We expect $\text{SNR} = \sqrt{N_k}$ for a Gaussian random field where N_k is the number of Fourier modes in each k bin. We find that non-Gaussianity is important at high SNR where it imposes an upper limit $[\text{SNR}]_l$. For a fixed volume V , it is not possible to achieve $\text{SNR} > [\text{SNR}]_l$ even if N_k is increased. The value of $[\text{SNR}]_l$ falls as reionization proceeds, dropping from ~ 500 at $\bar{x}_{\text{H I}} = 0.8\text{--}0.9$ to ~ 10 at $\bar{x}_{\text{H I}} = 0.15$ for a $[150.08 \text{ Mpc}]^3$ simulation. We show that it is possible to interpret $[\text{SNR}]_l$ in terms of the trispectrum, and we expect $[\text{SNR}]_l \propto \sqrt{V}$ if the volume is increased. For $\text{SNR} \ll [\text{SNR}]_l$ we find $\text{SNR} = \sqrt{N_k}/A$ with $A \sim 0.95\text{--}1.75$, roughly consistent with the Gaussian prediction. We present a fitting formula for the SNR as a function of N_k , with two parameters A and $[\text{SNR}]_l$ that have to be determined using simulations. Our results are relevant for predicting the sensitivity of different instruments to measure the EoR 21-cm power spectrum, which till date have been largely based on the Gaussian assumption.

Key words: methods: statistical, cosmology: theory, cosmology: dark ages, reionization, first stars, cosmology: diffuse radiation

1 INTRODUCTION

Observations of the redshifted 21-cm signal from neutral hydrogen (H I) are a very promising probe of the Epoch of Reionization (EoR), and there is a considerable observational effort underway to detect the EoR 21-cm power spectrum e.g. GMRT¹ (Paciga et al., 2013), LOFAR² (Yatawatta et al., 2013; van Haarlem et al., 2013), MWA³ (Tingay et al., 2013; Bowman et al., 2013), and PAPER⁴ (Parsons et al., 2014; Jacobs et al., 2014). Observing the EoR 21-cm signal is one of the key scientific goals of the future telescope SKA⁵ (Mellema et al., 2013). It is important to have quantitative predictions of both, the expected EoR 21-cm power

spectrum and the sensitivity of the different instruments to measure the expected signal.

On the theoretical and computational front, a considerable amount of effort has been devoted to simulate the expected EoR 21-cm signal (e.g. Gnedin 2000; Zahn et al. 2005; Mellema et al. 2006; Trac & Cen 2007; Thomas et al. 2009; Battaglia et al. 2013). There also have been several works to quantify the sensitivity to the EoR signal for different instruments (e.g. Morales 2005; McQuinn et al. 2006). Beardsley et al. (2013), Jensen et al. (2013) and Pober et al. (2014) have recently made quantitative predictions for detecting the EoR 21-cm power spectrum with the MWA, LOFAR, SKA and PAPER respectively.

The sensitivity of any instrument to the EoR 21-cm power spectrum is constrained by the errors, a part of which arises from the system noise of the instrument and another component which is inherent to the signal that is being detected (cosmic variance). It is commonly assumed, as in all the sensitivity estimates mentioned earlier, that the system noise and the EoR 21-cm signal are both independent Gaussian random variables. This is a reasonably good assumption

* rm@phy.iitkgp.ernet.in

† somnath@phy.iitkgp.ernet.in

¹ <http://www.gmrt.ncra.tifr.res.in>

² <http://www.lofar.org/>

³ <http://www.haystack.mit.edu/ast/arrays/mwa/>

⁴ <http://eor.berkeley.edu/>

⁵ <http://www.skatelescope.org/>

at large scales in the early stages of reionization when the H I is expected to trace the dark matter. Ionized bubbles, however, introduce non-Gaussianity (Bharadwaj & Pandey, 2005) and the 21-cm signal is expected to become highly non-Gaussian as the reionization proceeds. This transition in the 21-cm signal is clearly visible in Figure 1.

In this *Letter* we use semi-numerical simulations of the EoR 21-cm signal to study the effect of non-Gaussianities on the error estimates for the 21-cm power spectrum. Not only is this important for correctly predicting the sensitivity of the different instruments, it is also important for correctly interpreting the observation once an actual detection has been made. The entire analysis here focuses on the errors which are intrinsic to the 21-cm signal, and we do not consider the system noise corresponding to any particular instrument.

Throughout the *Letter*, we have used the Planck+WP best fit values of cosmological parameters $\Omega_{m0} = 0.3183$, $\Omega_{\Lambda 0} = 0.6817$, $\Omega_{b0}h^2 = 0.022032$, $h = 0.6704$, $\sigma_8 = 0.8347$, and $n_s = 0.9619$ (Planck Collaboration et al., 2013).

2 SIMULATING THE 21-CM MAPS

The evolution of the mass averaged neutral fraction $\bar{x}_{\text{H I}}(z)$ during EoR is largely unconstrained. Instead of choosing a particular model for $\bar{x}_{\text{H I}}(z)$, we have fixed the redshift $z = 8$ and considered different values of $\bar{x}_{\text{H I}}$ at an interval of 0.1 in the range $1.0 \geq \bar{x}_{\text{H I}} \geq 0.3$ in addition to $\bar{x}_{\text{H I}} = 0.15$. For each value of $\bar{x}_{\text{H I}}$ we have simulated 21 statistically independent realizations of the 21-cm map which were used to estimate the mean $P_b(k)$ and the rms. fluctuation (error) $\delta P_b(k)$ of the 21-cm power spectrum. We have used these to study how $P_b(k)$ and particularly $\delta P_b(k)$ evolve as reionization proceeds *i.e.* $\bar{x}_{\text{H I}}$ decreases.

The simulations are based on three main steps: (1.) determine the dark matter distribution at the desired redshift, (2.) identify the collapsed halos (3.) generate the reionization map using an excursion set formalism (Furlanetto et al., 2004) under the assumption that the collapsed halos host the ionizing sources and the hydrogen exactly traces the dark matter.

We have used a particle-mesh N-body code to simulate the $z = 8$ dark matter distribution in a $V_1 = [150.08 \text{ Mpc}]^3$ comoving volume with a 2144^3 grid using 1072^3 dark matter particles. The standard Friends-of-Friends (FoF) algorithm was used to identify collapsed dark matter halos from the output of the N-body simulation. We have used a fixed linking length 0.2 times the mean inter-particle separation, and require a halo to have at least 10 particles which corresponds to a minimum halo mass of $7.3 \times 10^8 h^{-1} M_\odot$.

We have assumed that the number of ionizing photons from a collapsed halo is proportional to its mass. It is possible to achieve different values of $\bar{x}_{\text{H I}}$ by appropriately choosing this proportionality factor. The ionizing photon field was used to construct the hydrogen ionization fraction and the H I distribution using the homogeneous recombination scheme of Choudhury et al. (2009). Following Majumdar, Bharadwaj & Choudhury (2013), the simulated H I distribution was mapped to redshift space to generate the 21-cm maps. The steps outlined in this paragraph used

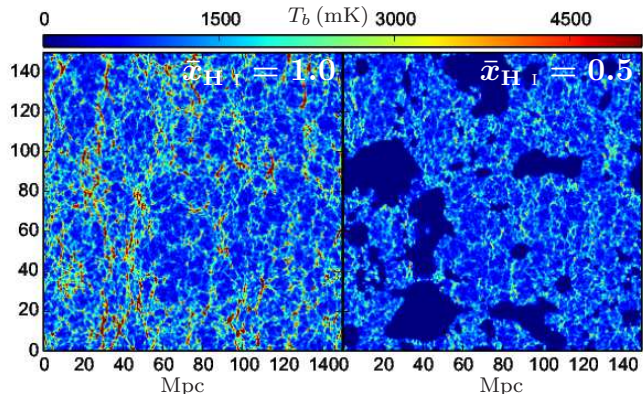


Figure 1. A section through one of the simulated redshift space H I brightness temperature maps for $\bar{x}_{\text{H I}} = 1.0$ (left) which is largely a Gaussian random field, and $\bar{x}_{\text{H I}} = 0.5$ (right) which has considerable non-Gaussianity due to the discrete ionized bubbles visible in the image. The redshift space distortion is with respect to a distant observer located along the horizontal axis.

a low resolution grid 8 times coarser than the N-body simulations.

Figure 1 shows a section through one of the simulated three dimensional 21-cm maps with $\bar{x}_{\text{H I}} = 1$ and 0.5 in the left and right panels respectively. The brightness temperature $T_b(\mathbf{x})$ is to a good approximation a Gaussian random field for $\bar{x}_{\text{H I}} = 1$. The homogeneous recombination scheme implemented here predicts an “inside-out” reionization where the high density regions are ionized first and the low density regions later. The image at $\bar{x}_{\text{H I}} = 0.5$ is dominated by several ionized bubbles which preferentially mask out the high density regions, the low density regions are left untouched. We expect the statistics of $T_b(\mathbf{x})$, or equivalently $\tilde{T}_b(\mathbf{k})$ its Fourier transform, to show considerable deviations from the original Gaussian distribution. The induced non-Gaussianity will reflect in the sizes and distribution of the ionized bubbles and we expect the non-Gaussianity to increase as reionization proceeds.

3 RESULTS

Figure 2 shows the brightness temperature fluctuation $\Delta_b^2(k) = k^3 P_b(k)/2\pi^2$ as a function of k for different values of $\bar{x}_{\text{H I}}$. The average power spectrum $P_b(k)$ and the $1 - \sigma$ errors $\delta P_b(k)$ were calculated using 21 independent realizations of the simulation, and the k range has been divided into 10 equally spaced logarithmic bins. Note the change in $\Delta_b^2(k)$ as reionization proceeds. At $\bar{x}_{\text{H I}} \sim 0.5$, the non-Gaussian Poisson noise of the discrete ionized regions makes a considerable contribution to $\Delta_b^2(k)$ at length-scales that are larger than the typical bubble radius. The ionized regions percolate at smaller $\bar{x}_{\text{H I}}$ where the Poisson noise of the surviving discrete H I regions makes a considerable contribution to $\Delta_b^2(k)$. While these effects have an imprint on the predicted $\Delta_b^2(k)$, the power spectrum does not capture the fact that the predicted signal is non-Gaussian. The error estimates for the power spectrum, however, are affected by the non-Gaussianity of the 21-cm signal.

We expect the signal to noise ratio to follow $\text{SNR} = P_b(k)/\delta P_b(k) = \sqrt{N_k}$ if the 21-cm signal is a Gaussian ran-

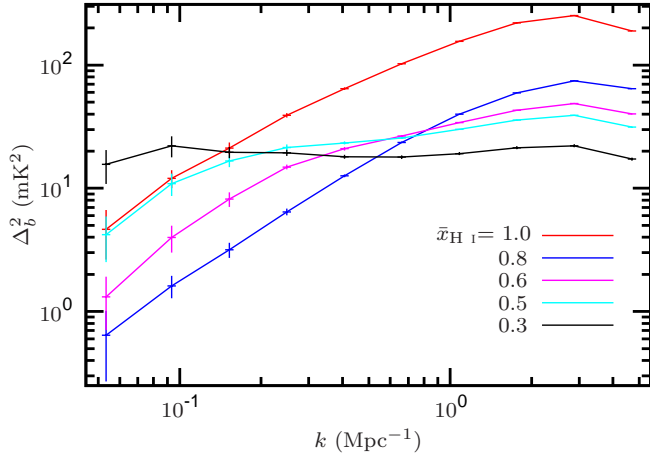


Figure 2. The mean squared 21-cm brightness temperature fluctuations $\Delta_b^2(k)$ and its $1 - \sigma$ error bars for the $\bar{x}_{H\text{ I}}$ values shown in the figure.

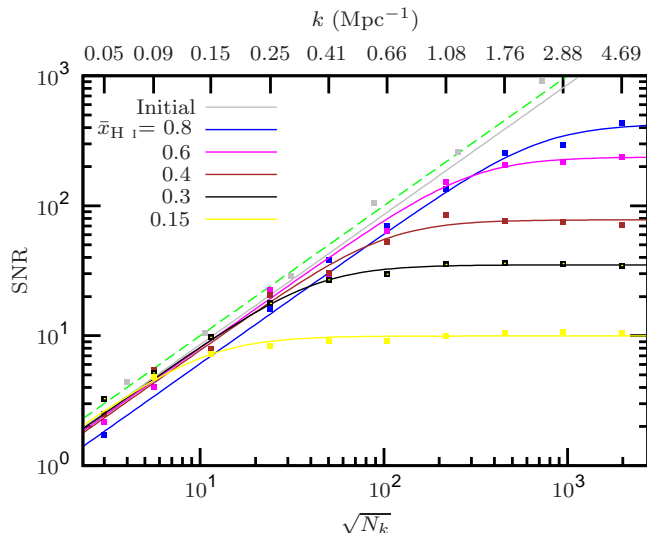


Figure 3. This shows the SNR as a function of $\sqrt{N_k}$. The 45° dashed line shows the SNR expected for a Gaussian random field, and ‘Initial’ refers to the input linear density fluctuations used for the dark matter N-body simulations. For the $\bar{x}_{H\text{ I}}$ values mentioned in the figure, the data points (squares) show the simulated SNR and the solid lines show the fit given by eq. (1). We have used 10 equally spaced logarithmic bins, and the k value corresponding to each bin is shown in the top x axis.

dom field, N_k here is the number of Fourier modes in each k bin. We have tested the Gaussian assumption by plotting the simulated SNR as a function of $\sqrt{N_k}$ in Figure 3 where the 45° dashed line shows the values expected for a Gaussian random field. We see that the input linear power spectrum used in the dark matter N-body simulations follows this over the entire range. In contrast, the SNR for the 21-cm power spectrum shows a different behaviour. For $\bar{x}_{H\text{ I}} \geq 0.3$ we find the expected $\text{SNR} \propto \sqrt{N_k}$ behaviour at $\text{SNR} \leq 10$, however the SNR values are 0.95–1.75 times than those predicted for a Gaussian random field. For larger SNR it increases slower than $\sqrt{N_k}$ and finally saturates at a limiting value $[\text{SNR}]_l$. The limiting value $[\text{SNR}]_l$ decreases as reionization proceeds ($\bar{x}_{H\text{ I}}$ falls). We do not explicitly see the $\text{SNR} \propto \sqrt{N_k}$ behaviour for $\bar{x}_{H\text{ I}} = 0.15$, this possibly exists at $\text{SNR} < 1$

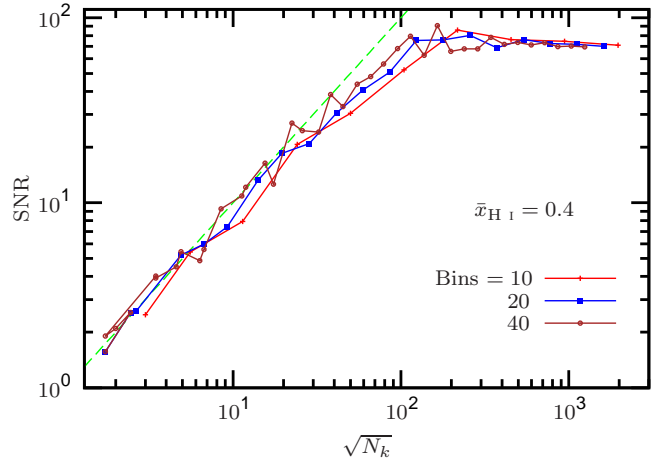


Figure 4. For $\bar{x}_{H\text{ I}} = 0.4$, this shows the simulated SNR as a function of $\sqrt{N_k}$ for 10, 20 and 40 equally spaced logarithmic bins.

which is outside the range that we have considered. In this case the SNR values are close to $[\text{SNR}]_l$ for the entire range that we have considered.

The equally spaced logarithmic bins that we have used imply a relation $N_k = Ck^3$ between N_k and k (where C is a constant), and the corresponding k values are shown on the upper x axis of Figure 3. It is therefore plausible that, in addition to $\bar{x}_{H\text{ I}}$, the deviations from the Gaussian predictions may also depend on k . To test this we have also considered 20 and 40 equally spaced logarithmic bins (Figure 4). The relation between N_k and k changes (*i.e.* the value of C changes) if we change the number of bins, however we find that curves showing the SNR as a function of N_k do not change. We therefore conclude that the effect of the non-Gaussianity on the SNR (or equivalently $\delta P_b(k)/P_b(k)$) does not depend on k , it depends only on $\bar{x}_{H\text{ I}}$ and N_k .

We find that the function

$$\text{SNR} = \frac{\sqrt{N_k}}{A} \left[1 + \frac{N_k}{(A[\text{SNR}]_l)^2} \right]^{-0.5} \quad (1)$$

provides a good fit to the simulated SNR. For each value of $\bar{x}_{H\text{ I}}$, we have used a least-square fit to obtain the best fit A and $[\text{SNR}]_l$. The solid curves in Figure 3 show the fit to the SNR given by eq. (1) using the best fit parameters. Figure 5 shows the best fit parameters A and $[\text{SNR}]_l$ as a function of $\bar{x}_{H\text{ I}}$. The parameter A quantifies the deviation from the Gaussian prediction in the low SNR regime ($\text{SNR} \ll [\text{SNR}]_l$) where we have $\text{SNR} = \sqrt{N_k}/A$. We find that the value of A increases from $A \sim 0.95$ at $\bar{x}_{H\text{ I}} = 0.15$ to $A \sim 1.75$ at $\bar{x}_{H\text{ I}} = 0.9$. Surprisingly, in this regime the SNR approaches the Gaussian prediction as the reionization proceeds. In contrast, the value of $[\text{SNR}]_l$ decreases by a factor of ~ 50 as the $\bar{x}_{H\text{ I}}$ falls from 0.9 to 0.15. The deviations from the Gaussian predictions seen at large SNR increase as reionization proceeds.

4 MODELLING THE SNR.

The power spectrum $P_b(k)$ and the trispectrum $T_b(\mathbf{k}_1, \mathbf{k}_2, \mathbf{k}_3, \mathbf{k}_4)$ of the brightness temperature fluctuations

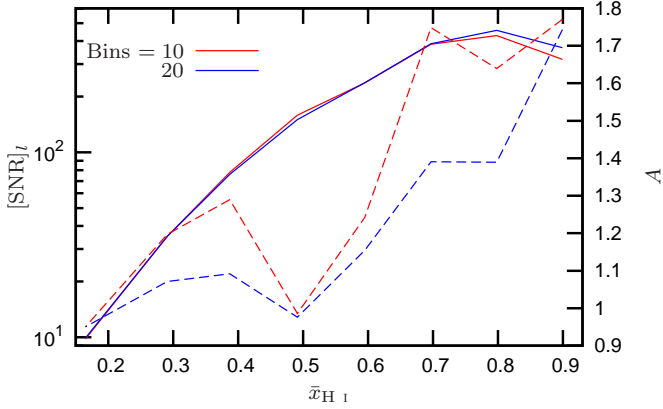


Figure 5. This shows how the best fit parameters A (dashed) and $[\text{SNR}]_l$ (solid) vary with $\bar{x}_{\text{H I}}$. The results are shown for 10 and 20 equally spaced logarithmic bins.

$\tilde{T}_b(a) \equiv \tilde{T}_b(\mathbf{k}_a)$ are respectively defined through

$$\langle \tilde{T}_b(a)\tilde{T}_b(b) \rangle = V\delta_{a+b,0}P_b(a) \quad (2)$$

and

$$\begin{aligned} \langle \tilde{T}_b(a)\tilde{T}_b(b)\tilde{T}_b(c)\tilde{T}_b(d) \rangle &= V^2[\delta_{a+b,0}\delta_{c+d,0}P_b(a)P_b(c) \\ &+ \delta_{a+c,0}\delta_{b+d,0}P_b(a)P_b(b) + \delta_{a+d,0}\delta_{b+c,0}P_b(a)P_b(b)] \\ &+ V\delta_{a+b+c+d,0}T_b(a,b,c,d) \end{aligned}$$

where V refers to the comoving volume of the region under consideration and $\langle \dots \rangle$ denotes an ensemble average over different realizations of the fluctuations. We use these to calculate the mean and the variance of the binned power spectrum estimator which we define as

$$\hat{P}_b(k) = (N_k V)^{-1} \sum_a \tilde{T}_b(a)\tilde{T}_b(-a), \quad (3)$$

where the sum \sum_a extends over all the Fourier modes \mathbf{k}_a within the bin, and k is the representative comoving wave number for the bin. The bins here are spherical shells of width Δk (which varies from bin to bin). The modes \mathbf{k}_a and $-\mathbf{k}_a$ do not give independent estimates of the power spectrum. We restrict the sum \sum_a to half the spherical shell, and N_k refers to the number of Fourier modes in this volume.

We then have

$$\langle \hat{P}_b(k) \rangle = \bar{P}_b(k) = (N_k)^{-1} \sum_a P_b(a) \quad (4)$$

which is the bin averaged power spectrum, and the variance

$$\langle [\delta \hat{P}_b(k)]^2 \rangle = [\delta P_b(k)]^2 = (N_k)^{-1} \overline{P_b^2(k)} + V^{-1} \bar{T}_b(k,k) \quad (5)$$

where

$$\overline{P_b^2(k)} = (N_k)^{-1} \sum_a P_b^2(a) \quad (6)$$

and

$$\bar{T}_b(k,k) = (N_k)^{-2} \sum_{a,b} T_b(a,-a,b,-b) \quad (7)$$

are the square of the power spectrum and the trispectrum respectively averaged over the bin.

The $\text{SNR} \equiv \bar{P}_b(k)/[\delta P_b(k)]$ can be cast in the form of eq. (1) provided we identify

$$A = \sqrt{\frac{\overline{P_b^2(k)}}{[\bar{P}_b(k)]^2}} \quad (8)$$

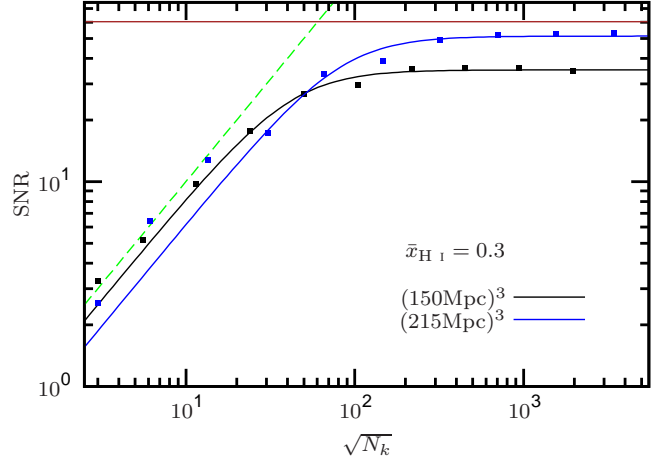


Figure 6. This shows a comparison of the results from simulations with two different box sizes, for a fixed $\bar{x}_{\text{H I}} = 0.3$. The solid curves show eq. (1) with the best fit parameters for the respective data points (squares). The horizontal solid line shows $[\text{SNR}]_l$ for the smaller volume scaled by the factor $\sqrt{V_2/V_1}$, and the dashed line shows $\text{SNR} = \sqrt{N_k}$.

and

$$[\text{SNR}]_l = \sqrt{\frac{[\bar{P}_b(k)]^2 V}{\bar{T}_b(k,k)}} \quad (9)$$

Our calculation (eq. 8) shows that A arises from the fact that the power spectrum varies across the different Fourier modes which contribute to a bin. This implies that $\overline{P_b^2(k)} > [\bar{P}_b(k)]^2$ whereby $A > 1$ even for a purely Gaussian random field. This explains why the SNR values for the ‘Initial’ Gaussian random field (Figure 3) are lower than those predicted by $\text{SNR} = \sqrt{N_k}$, even though both have the same slope.

The limiting SNR (eq. 9) depends on the trispectrum. Considering a Gaussian random field first, the statistics are completely specified by the power spectrum and $T_b(\mathbf{k}_1, \mathbf{k}_2, \mathbf{k}_3, \mathbf{k}_4) = 0$. We expect $\text{SNR} = \sqrt{N_k}/A$ to hold throughout in this case. However, the brightness temperature fluctuations become increasingly non-Gaussian as reionization proceeds. We expect a non-zero trispectrum to develop and increase as reionization proceeds. This is borne out by Figure 5 where $[\text{SNR}]_l$ is found to fall as $\bar{x}_{\text{H I}}$ declines. Our results (Figure 4) also indicate that the ratio $[\bar{P}_b(k)]^2/\bar{T}_b(k,k) \propto [\text{SNR}]_l^2$ is roughly independent of k , at least over the k range accessible through rebinning the data in the figure. Finally, eq. (9) implies that we expect the limiting SNR to scale as $[\text{SNR}]_l \propto \sqrt{V}$ with the simulation volume.

We have investigated the volume dependence of the SNR by carrying out 21 independent realizations of a larger simulation with comoving volume $V_2 = [215 \text{ Mpc}]^3$, maintaining the same spatial resolution as in Section 2. Figure 6 shows a comparison of the SNR between the smaller (V_1) and the larger (V_2) simulations for $\bar{x}_{\text{H I}} = 0.3$. In both cases the power spectrum was evaluated in 10 equally spaced logarithmic bins. Note that the Fourier modes, N_k and k corresponding to the 10 bins are different in the two sets of simulations which are being compared. The results for the larger simulation are qualitatively similar to those for the

smaller one, though the SNR values are different. We find that the functional form given by eq. (1) does not provide a very good fit at small N_k for the larger simulation. This is possibly because the value of A (eq. 8) varies from bin to bin. The fit, however, is very good at large N_k where the behaviour is dominated by $[\text{SNR}]_l$. The horizontal solid line in the figure shows $[\text{SNR}]_l$ for the smaller simulation scaled by the factor $\sqrt{V_2/V_1}$. We find that $[\text{SNR}]_l$ calculated from the larger simulation is roughly consistent with this solid line. This validates the $[\text{SNR}]_l \propto \sqrt{V}$ dependence predicted by eq. (9). We find similar results for the other values of $\bar{x}_{\text{H I}}$ not shown here.

5 DISCUSSION AND CONCLUSIONS

We may think of the EoR 21-cm signal as a combination of two components, one a Gaussian random field and another a non-Gaussian component from the discrete ionized bubbles. The picture is slightly changed as the reionization proceeds and the ionized regions percolate. The non-Gaussian component then arises from the discrete H I clumps. The Gaussian components in the different Fourier modes $\tilde{T}_b(\mathbf{k})$ are independent, the non-Gaussian components however are correlated - this being quantified through the bispectrum (Bharadwaj & Pandey, 2005), trispectrum etc. The contribution to $\delta P_b(k)/P_b(k)$ from the Gaussian component comes down as $1/\sqrt{N_k}$, whereas the non-Gaussian contribution remains fixed even if N_k is increased. The Gaussian assumption gives a reasonable description at low SNR, the non-Gaussian contribution however sets an upper limit $[\text{SNR}]_l$. For a fixed volume V , it is not possible to increase the SNR beyond $[\text{SNR}]_l$ by combining the signal from more Fourier modes. The non-Gaussianity increases as reionization proceeds, and $[\text{SNR}]_l$ falls from ~ 500 at $\bar{x}_{\text{H I}} = 0.8 - 0.9$ to ~ 10 at $\bar{x}_{\text{H I}} = 0.15$ for the $[150.08 \text{ Mpc}]^3$ simulations.

The limiting signal to noise ratio $[\text{SNR}]_l$ is proportional to \sqrt{V} , and it is possible to achieve a high SNR by increasing the volume. The value of $\sqrt{N_k}$ in eq. (1), however, also scales as $\propto \sqrt{V}$ for a fixed bin width Δk . Although it is possible to increase the SNR by increasing the volume, the relative contribution from the non-Gaussianity ($[\tilde{P}_b(k)]^2/\tilde{T}_b(k, k)$) does not vary with V .

In the present analysis we have used a simple model of reionization, and held $z = 8$ fixed. The predictions will be different if effects like inhomogeneous recombination are included, and the evolution of $\bar{x}_{\text{H I}}$ with z is taken into account. The present work highlights the fact that non-Gaussian effects could play an important role in the error predictions for the EoR 21-cm power spectrum. We plan to consider the implications for the different EOR experiments in future work.

References

Battaglia, N., Trac, H., Cen, R., & Loeb, A. 2013, ApJ, 776, 81
 Beardsley, A. P. 2013, MNRAS, 429, L5
 Bharadwaj, S., & Pandey, S. K. 2005, MNRAS, 358, 968
 Bowman, J. D., Cairns, I., Kaplan, D. L., et al. 2013, Pub. Astro. Soc. Australia, 30, 31

Choudhury, T. R., Haehnelt, M. G., & Regan, J. 2009, MNRAS, 394, 960
 Furlanetto, S. R., Zaldarriaga, M. & Hernquist, L. 2004, ApJ, 613, 1
 Gnedin, N. Y. 2000, ApJ, 535, 530
 Jacobs, D. C., Pober, J. C., Parsons, A. R., et al. 2014, arXiv:1408.3389
 Jensen, H., Datta, K. K., Mellema, G., et al. 2013, MNRAS, 435, 460
 Majumdar, S., Bharadwaj, S., & Choudhury, T. R. 2013, MNRAS, 434, 1978
 McQuinn, M., Zahn, O., Zaldarriaga, M., Hernquist, L., & Furlanetto, S. R. 2006, ApJ, 653, 815
 Mellema, G., Iliev, I. T., Pen, U.-L., & Shapiro, P. R. 2006, MNRAS, 372, 679
 Mellema, G., Koopmans, L. V. E., Abdalla, F. A., et al. 2013, Experimental Astronomy, 36, 235
 Morales, M. F. 2005, ApJ, 619, 678
 Paciga, G., Albert, J. G., Bandura, K., et al. 2013, MNRAS, 433, 639
 Parsons, A. R., Liu, A., Aguirre, J. E., et al. 2014, ApJ, 788, 106
 Planck Collaboration, Ade, P. A. R., Aghanim, N., et al. 2013, arXiv:1303.5076
 Pober, J. C., Liu, A., Dillon, J. S., et al. 2014, ApJ, 782, 66
 Thomas, R. M., Zaroubi, S., Ciardi, B., et al. 2009, MNRAS, 393, 32
 Tingay, S. J., Goeke, R., Bowman, J. D., et al. 2013, Pub. Astro. Soc. Australia, 30, 7
 Trac, H., & Cen, R. 2007, ApJ, 671, 1
 van Haarlem, M. P., Wise, M. W., Gunst, A. W., et al. 2013, AAP, 556, A2
 Yatawatta, S., de Bruyn, A. G., Brentjens, M. A., et al. 2013, AAP, 550, A136
 Zahn, O., Zaldarriaga, M., Hernquist, L., & McQuinn, M. 2005, ApJ, 630, 657